

# Flexible Asymmetric Supercapacitors using Mildly Etched $\text{Ti}_3\text{C}_2\text{T}_x$ MXene for Powering Wearable Devices

Anamika Ashok, Varsha Vijayan, Shalu Mariam George, Aleena Tomy,  
Asha Arackal Sukumaran,\* Oleksii Klymov, Vicente Muñoz-Sanjose,  
Mahesh Eledath Changarath, and Juan F. Sánchez Royo

The work proposes a novel and fast method to synthesize  $\text{Ti}_3\text{C}_2\text{T}_x$  MXene with enhanced redox activity and improved structural, optical, and electronic properties by incorporating NaOH in the late etching stage. The technique eliminates the need for post-etching delamination while maintaining the properties of delaminated MXene. Optimizing the concentration of NaOH leads to the removal of the unetched MAX phase from MXene in the mild *in situ* HF etching technique. The obtained ultrapure MXene is used as the negative electrode in an asymmetric supercapacitor device configuration. The MXene// $\text{RuO}_2$  asymmetric device showed superior electrochemical performance with a specific capacitance

of  $73.3 \text{ F g}^{-1}$ , energy density of  $23 \text{ Wh kg}^{-1}$ , and power density of  $796 \text{ W kg}^{-1}$ , with potential extendable up to 1.5 volts. The device retained more than 90% of its performance at the end of 2000 cycles. The all-solid-state asymmetric supercapacitor device fabricated using PVA/ $\text{H}_2\text{SO}_4$  gel polymer as the electrolyte, and Na-MX and  $\text{RuO}_2$  as the electrodes gave a specific capacitance of  $845 \text{ mF g}^{-1}$ , energy density of  $470 \text{ mWh kg}^{-1}$ , and power density of  $5000 \text{ mW kg}^{-1}$  at a current density of  $5 \text{ mA g}^{-1}$  with an extendable voltage window up to 2 V, more than twice the window obtained using symmetric supercapacitor with MXene as electrode.

## 1. Introduction

Titanium carbide ( $\text{Ti}_3\text{C}_2\text{T}_x$ ) is a member of the 2D transition metal carbides/nitrides family called MXenes. The surface-terminating functional groups impart high conductivity, surface area, and good hydrophilicity to  $\text{Ti}_3\text{C}_2\text{T}_x$  MXene.<sup>[1]</sup>  $\text{Ti}_3\text{C}_2\text{T}_x$  MXene is usually synthesized from  $\text{Ti}_3\text{AlC}_2$  MAX phase via the HF etching technique, which is a rigorous reaction, involving a high concentration

of HF.<sup>[2]</sup> A milder *in situ* HF-forming etching technique is an alternative to this strategy. However, the *in situ* HF forming technique does not completely remove the Al from the MAX phase ( $\text{Ti}_3\text{AlC}_2$ ) during etching. Hence, several researchers have been trying to modify the HF etching technique by introducing additional etchants like alkalis and acids, which will reduce the concentration of HF being used.<sup>[3–5]</sup> However, attempts to improve the *in situ* HF forming technique to enhance the properties of MXene and to eliminate the unetched MAX phase from the system have been rare. The present work attempts this uncommon route, modification of the *in situ* HF forming etching route using NaOH. Zhang et al. have reported on a two-step modification technique using  $\text{FeCl}_3$  to improve the HF etching technique, where the metal cations displace the Al to improve the properties of MXene, while maintaining the concentration of HF to a minimum.<sup>[6]</sup> A similar improvement in the purity of MXene has been obtained in the present work by appropriately adjusting the concentration of NaOH without hampering the crystallinity of the system. Hydrothermal synthesis of MXene using 27.5 M NaOH was carried out by Li et al. at a temperature of 180 °C.<sup>[7]</sup> This fluorine-free etching technique, however, resulted in the oxidation of MXene to form titanium dioxide ( $\text{TiO}_2$ ). Moreover, a complete removal of Al was not possible, despite the high temperature and high alkali concentration.<sup>[7]</sup> Hence, the merit of the present work lies in the use of a low concentration of NaOH to assist the *in situ* HF forming technique, in removing Al almost completely, without affecting the inherent properties of the material. The proposed work also improves the redox behavior of the multilayer MXene, eliminating the additional delamination steps, maintaining the scalability of the reaction. This approach is also quite

A. Ashok, V. Vijayan, S. M. George, A. Tomy, A. Arackal Sukumaran  
Nanomaterials for Emerging Solid-state Technology (NEST) Research Laboratory

Department of Physics  
Cochin University of Science and Technology  
Cochin, Kerala 682022, India  
E-mail: asa@cusat.ac.in

A. Arackal Sukumaran  
Centre of Excellence in Advanced Materials  
Cochin University of Science and Technology  
Cochin, Kerala 682022, India

A. Arackal Sukumaran  
Inter University Centre for Nanomaterials and Devices (IUCND)  
Cochin University of Science and Technology  
Cochin, Kerala 682022, India

O. Klymov, V. Muñoz-Sanjose  
Department of Applied Physics and Electromagnetism  
University of Valencia  
c/ Dr. Moliner n° 50, 46100 Burjassot, Spain

M. E. Changarath, J. F. Sánchez Royo  
Institute of Materials Science (ICMUV)  
University of Valencia  
c/ Catedrático José Beltrán, 46980 Paterna, Spain

 Supporting information for this article is available on the WWW under <https://doi.org/10.1002/batt.202500389>

novel considering the reports of tedious and unscalable routes for delaminating  $Ti_3C_2T_x$  to improve the redox activity.<sup>[8]</sup>

The inherent redox activity makes MXene an ideal choice for use as an electrode material in energy storage applications like supercapacitors.<sup>[8–10]</sup> As energy storage devices, supercapacitors have gained immense attention due to their fast reversible redox reactions, long cyclability, and the increasing demand to complement the intermittent nature of renewable energy sources.<sup>[11–13]</sup> One of the important performance metrics of a supercapacitor, which researchers worldwide are trying to improve, is its energy density.<sup>[14–16]</sup> Energy density is directly dependent on the specific capacitance and the square of the potential of the system.<sup>[14]</sup> An improvement in material properties, like effective surface area and conductivity, can lead to an improvement in specific capacitance. The widening of the voltage window, however, depends on the choice of electrolyte. Symmetric supercapacitors working in aqueous electrolytes are limited by the thermodynamic potential for hydrogen evolution.<sup>[17–19]</sup> An asymmetric system, with each electrode working in a different window, makes it possible to extend the voltage window of the device beyond 1 V for aqueous electrolytes.<sup>[20–22]</sup> Moreover, since the energy density varies as the square of the potential, an extended window enhances the energy density of the device. Achieving a higher energy density by the use of aqueous asymmetric supercapacitor devices is a more environmentally benign option for real-life applications due to the higher ionic conductivity, smaller ionic size, reduced cost, high mobility, and nontoxicity of aqueous electrolytes, as compared to organic electrolytes.<sup>[22–24]</sup> In the present work, the NaOH-modified  $Ti_3C_2T_x$  MXene was used as the negative electrode. It was assembled against RuO<sub>2</sub> as a positive electrode for the fabrication of an asymmetric supercapacitor. RuO<sub>2</sub> is a conventional pseudocapacitive material, with proton-induced changes in the oxidation of Ru in aqueous electrolytes.<sup>[25,26]</sup> In our work, the MXene//RuO<sub>2</sub> device exhibited enhanced performance due to greater compatibility. To the best of our knowledge, this is the first report in the current literature on the enhanced removal of unetched MAX phase from MXene via NaOH-assisted in situ HF forming technique to obtain MXene with properties similar to delaminated MXene, without including any additional delamination processes, and its use in the fabrication of an asymmetric supercapacitor device. The work shows immense potential as a novel technique to obtain MXene of high quality, avoiding the complexity of the synthesis process and providing a scalable route.

## 2. Experimental Section

The schematic of the experimental process is shown in Figure 1. Lithium fluoride and hydrochloric acid (Alpha Aesar) were used to make the etching solution. MXene was prepared by etching the MAX phase precursor,  $Ti_3AlC_2$  (90%) obtained from Sigma Aldrich, by the in situ HF forming technique.<sup>[27]</sup> The in situ HF etching process involves the addition of 1 g of  $Ti_3AlC_2$  (purity > 90%, Sigma Aldrich) MAX phase powder to the etchant prepared by adding 1.6 g LiF to 20 mL 9 M HCl, at room temperature. For modification

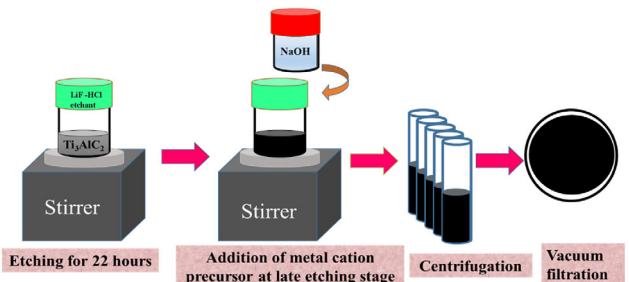


Figure 1. Schematic of the synthesis process of NaOH-modified MXene.

with NaOH, the addition of NaOH during the late etching stage, after 22 h of etching, at concentrations varying from 0.02 to 0.04 M, was done. The solution was then centrifuged until neutral pH and then vacuum filtered to obtain powder. The samples were named MX, 0.02 Na MX, 0.03 Na MX, and 0.04 Na MX. RuO<sub>2</sub> was synthesized by using the hydrothermal method from Ruthenium(III) chloride, as a precursor (Sigma Aldrich). The process for the RuO<sub>2</sub> synthesis from RuCl<sub>3</sub> is included in the Supporting Information. The specific capacitance, energy density, and power density were calculated using the following equations

$$C_m = \frac{\int IdV}{mv\Delta V} \quad (1)$$

$$E = \frac{1}{2} C \Delta V^2 \quad (2)$$

$$P = \frac{E}{\Delta t} \quad (3)$$

where  $m$  is the active mass of the electrode (g),  $\Delta V$  is the potential window (V),  $\Delta t$  is the discharge time (s), and  $I$  is the discharge current (A).

X-ray diffraction (XRD) patterns were obtained with a Rigaku MiniFlex X-ray diffractometer, utilizing the Cu K $\alpha$  radiation ( $\lambda = 1.54 \text{ \AA}$ ). Further, UV–Visible–near infrared (UV-Vis-NIR) spectra were recorded with a Jasco V-570 UV–Vis NIR spectrophotometer. Raman spectroscopy was done using a HORIBA MTB XPlora spectrometer equipped with 785 nm lasers and a HORIBA JOBIN YVON LabRAM HR Raman spectrometer with a 633 nm laser. A scanning electron microscope (SEM), HITACHI S4800, equipped with an X-ray detector, was employed to examine the morphology. XPS measurements were performed in a SPECS GmbH system (base pressure  $1 \times 10^{-10} \text{ mbar}$ ) equipped with an ASTRAIOS 190 2D-CMOS hemispherical analyzer. For the X-ray photoelectron spectroscopy (XPS) measurements, photoelectrons were excited with the Al K $\alpha$  line (1486.7 eV) of a monochromatic X-ray source [ $\mu$ FOCUS 500 (SPECS GmbH)]. Electrochemical measurements were performed using the electrochemical workstation CHI-6054E. Transmission electron microscopy (TEM) analysis was carried out using high-resolution TEM (HRTEM): Jeol/JEM 2100.

The electrode was prepared on carbon cloth obtained from Sainergy Fuel Cells Pvt Ltd. Carbon cloth was precleaned in acetone, ethanol, and deionized water. It was then dried at 100 °C and brush-coated with MXene ink by mixing Ti<sub>3</sub>C<sub>2</sub>T<sub>x</sub>, polyvinylidene difluoride, and carbon black in the ratio 90:5:5, using N-methyl pyrrolidone as the solvent, until the desired mass loading of 9 mg cm<sup>-2</sup> was obtained. The same process was followed for RuO<sub>2</sub>. The prepared working electrode was characterized against Ag/AgCl in a 3 M KCl reference electrode and a Pt mesh counter electrode in 3 M H<sub>2</sub>SO<sub>4</sub> electrolyte, in a three-electrode setup. The characterization of the asymmetric supercapacitor was done by using Swagelok cells with Ti<sub>3</sub>C<sub>2</sub>T<sub>x</sub> MXene as one of the electrodes and RuO<sub>2</sub> as the other electrode, with cellulose fiber as the separator in a 2-electrode configuration.

The PVA/H<sub>2</sub>SO<sub>4</sub> gel polymer electrolyte was prepared via a simple solution casting technique. 1 g PVA powder was added to 10 mL of deionized water at 95 °C. A vigorous stirring for 15–20 min was followed by a low-rpm stirring for 1 h, until the PVA dissolves completely and forms a gel. Subsequently, the temperature is turned off, and 800 μL of H<sub>2</sub>SO<sub>4</sub> is added to the PVA gel. Stirring is continued for another 15 min. The solution is then cast in a Petri dish and allowed to dry in a desiccator.

### 3. Results and Discussion

Figure 2 compares the XRD pattern of Ti<sub>3</sub>AlC<sub>2</sub> MAX phase precursor with Ti<sub>3</sub>C<sub>2</sub>T<sub>x</sub> MXene and NaOH-modified MXene, and (b) shows

the XRD pattern of Ti<sub>3</sub>C<sub>2</sub>T<sub>x</sub> MXene and NaOH-modified MXene around 39°. The success of etching in MXene was determined by the extent of loss of intensity of the Ti-Al peak around 39°, the most intense peak in the XRD pattern of MAX phase, as shown in Figure 2a.<sup>[28]</sup> A close inspection of the XRD of the samples indicates that, with an increase in concentration of NaOH, the intensity of the Ti-Al peak around 39° and that of the MAX phase around 9.6°, decreases. For a 0.04 M concentration of NaOH, both the MAX phase peak and the Ti-Al peak have been obtained. Moreover, the (002) plane diffraction peak of MXene around 6° has emerged with significant intensity. The intensification of the (002) plane diffraction peak and the loss of higher-order peaks are typical characteristics of delaminated MXene.<sup>[29]</sup> This means the addition of 0.04 M NaOH has resulted in inherent delamination of MXene, without resorting to any additional steps. Intercalation-assisted delamination is reported to result in the emergence of characteristic XRD peaks of MXene with superior intensity.<sup>[30]</sup>

Li et al. obtained a 92 wt% purity MXene via hydrothermal synthesis using 27.5 M NaOH.<sup>[31]</sup> In the present study, a very low concentration of NaOH-assisted in situ etching technique yielded a better-purity sample. The high purity of the synthesized MXene can be quantified using the following formula by Mashtalar et al., and the corresponding results are tabulated in Table 1.<sup>[32]</sup>

$$y = 1 - 0.2x + 0.013x^2 \quad (4)$$

where,  $y$  = weight fraction of Ti<sub>3</sub>C<sub>2</sub>T<sub>x</sub> MXene;  $x$  = ratio of (104) and (002) plane diffraction peaks in MXene.

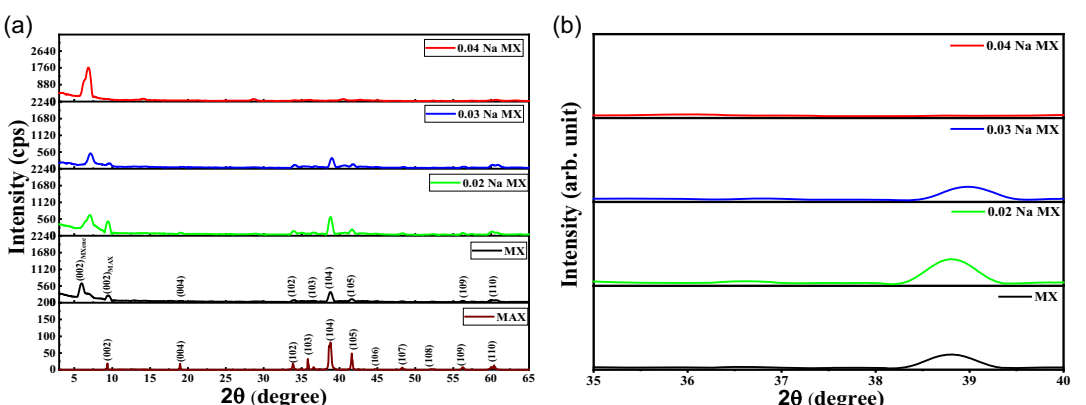


**Figure 2.** a) Comparison of XRD pattern of MAX phase precursor with MX and NaOH-modified samples. b) XRD pattern of MX- and NaOH-modified samples around 39°.

**Table 1.** A comparison of the fraction of MXene content formed in the samples prepared by modifying MXene using NaOH.

Sample	Peak position 2θ (degrees) of planes		Area under the peaks of planes		Intensity ratio of (104) to (002) [x]	MXene content [%] [y]
	(002)	(104)	(002)	(104)		
MX	6.6	39	482	385	0.79	85
0.02 Na MX	6.6	39	759	371	0.48	93.3
0.03 Na MX	6.6	39	701	208	0.29	94.3
0.04 Na MX	6.6	—	1009.5	—	—	100

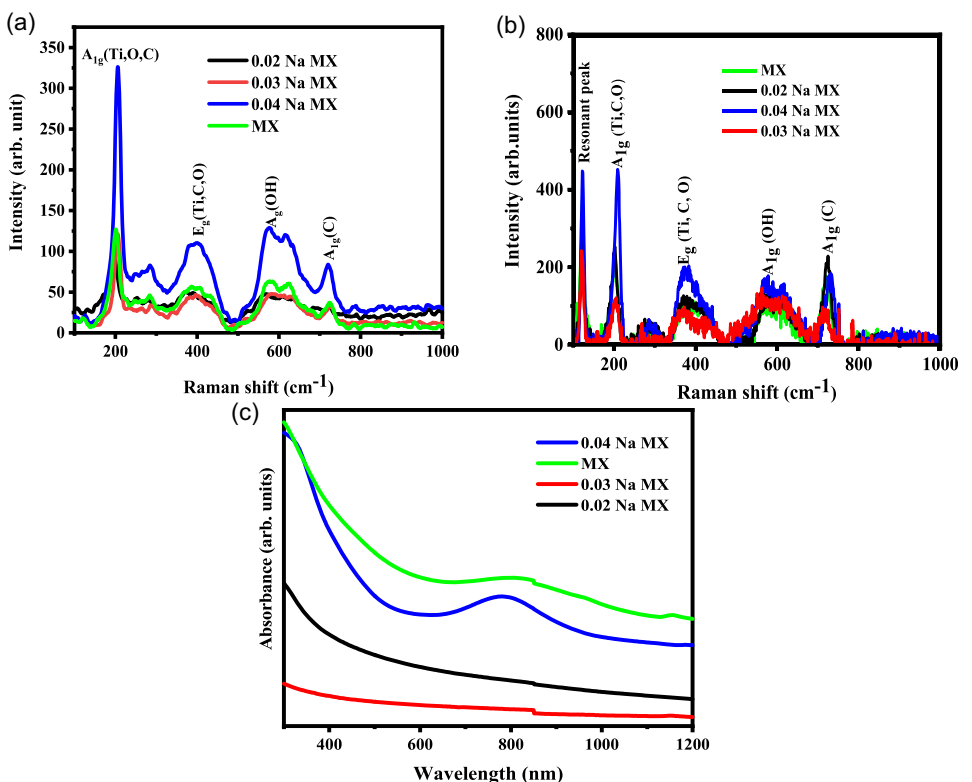


**Figure 3.** Comparison of the Raman spectrum of MX with all Na-modified samples using a) 633 nm laser, b) 785 nm laser, and c) UV-Vis NIR spectra of MX and Na MX samples.

The Raman spectra of all samples recorded using a 633 nm laser are shown in Figure 3a. The Raman spectrum of 0.04 Na MX shows the emergence of the A<sub>1g</sub> (Ti, O, C) peak due to the out-of-plane vibration of oxygen bonded onto titanium carbide at 202 cm<sup>-1</sup> with high intensity. This is suggestive of a lesser concentration of defects and a lesser relative rotation among the flakes. This is also an indication of higher ordering among the Ti and C layers, due to stronger vibration of the flake as a whole.<sup>[33]</sup> The Raman spectra also confirm the presence of oxygen functional groups. The absence of peaks corresponding to TiO<sub>2</sub> indicates the absence of partial oxidation in the prepared sample. The A<sub>1g</sub> out-of-plane vibrations of carbon occurring around 720 cm<sup>-1</sup> are a characteristic of the clay behavior of MXene. This indicates less restricted motion of MXene flakes surrounded by H<sub>2</sub>O molecules, in comparison with the dry powder. In a dry powder or powder with lower interlayer spacing, as in the case of HF-etched MXene powder, this peak occurs at 711 cm<sup>-1</sup> as a consequence of more restricted vibrations.<sup>[34]</sup>

The interband transition at 1.6 eV gives rise to a plasmonic resonance at 785 nm in the UV-Vis NIR spectra (Figure 3c). The resonant peak corresponding to this interband transition will be obtained at 120 cm<sup>-1</sup>.<sup>[34]</sup> This has translated into a resonant Raman peak at 120 cm<sup>-1</sup> when using a laser wavelength of 785 nm, as depicted in Figure 3b.<sup>[34]</sup>

The variation in the morphology of the MXene samples with the addition of NaOH is shown in Figure 4. For the pristine MXene sample, a compact morphology, as shown in Figure 4a, is

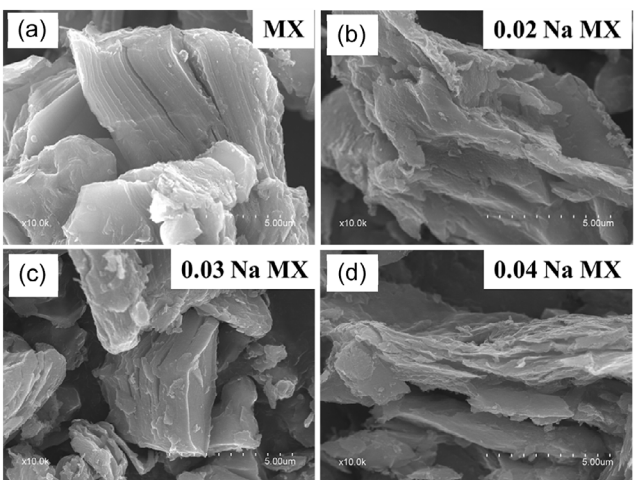


**Figure 4.** SEM image of a) MX, b) 0.02 Na MX, c) 0.03 Na MX, and d) 0.04 Na MX.

obtained. As the concentration of NaOH increases, the layers become more open. The SEM image of 0.04 Na MX exhibits a layered structure with thinner layers, as shown in Figure 4d and Figure S1 of the Supporting Information. Such thinning of layers is usually observed in MXenes etched for longer durations for the enhanced removal of Al.<sup>[35]</sup>

Hence, the formation of thin layers in the optimized sample indicates the success of the etching process.

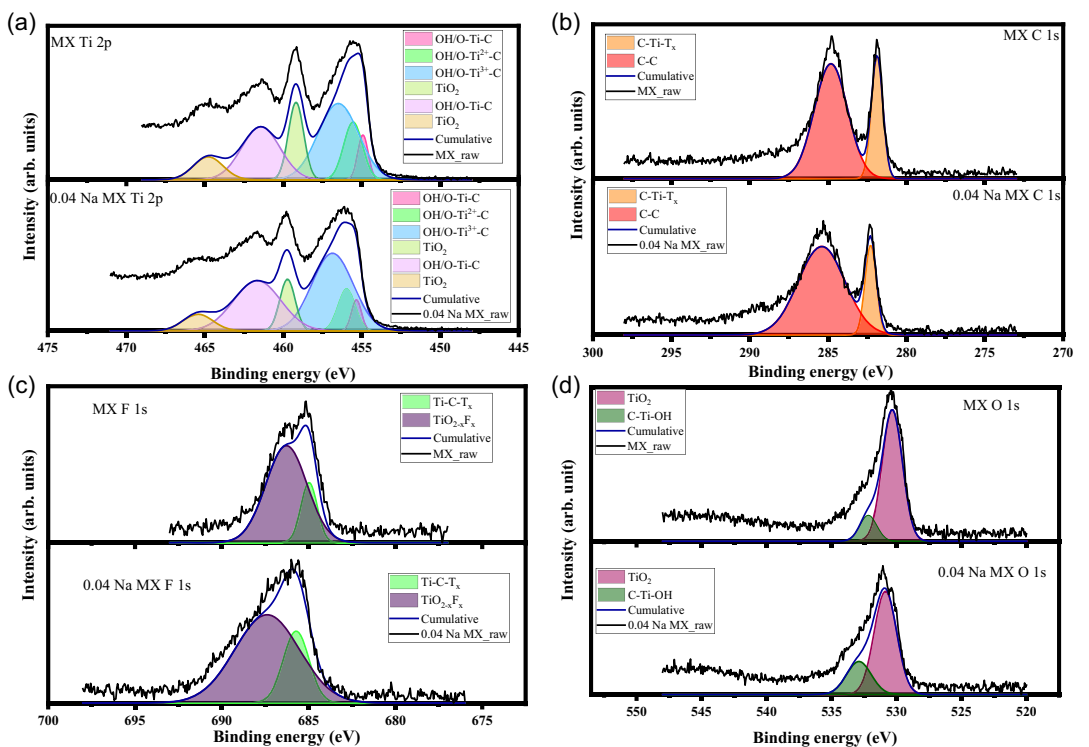


**Figure 5.** Comparison of a) Ti 2p, b) C 1s, c) F 1s, and d) O 1s XPS spectra of MX and 0.04 Na MX.

Therefore, an appropriate optimization of NaOH and its introduction during the in situ etching process has proved to be instrumental in the enhanced removal of Al. **Figure 5** shows a comparison of the XPS of MX and 0.04 Na MX, which shows the presence of —F, —OH, and =O functional groups in the prepared samples. The Ti 2p spectra (Figure 5a) show a lower degree of oxidation in the 0.04 Na MX sample, evident from the lower intensity of TiO<sub>2</sub> peaks, consistent with other characterizations. XPS, being a surface analytical technique, shows the presence of mild surface oxidation in the form of TiO<sub>2</sub>. However, since the effect of TiO<sub>2</sub> is not detected in other characterizations, such as Raman spectroscopy, the oxidation detected via XPS may be treated as a mild surface phenomenon, consistent with other reported literature.<sup>[36]</sup> It is also a notable fact that the 100% purity obtained from XRD can only be assumed as a relative quantification of purity among the different samples prepared, and the purity refers to the formation of MXene without remnant MAX phase.

Moreover, the Al 2p signal is less prominent in the Na MX sample (Figure S2a of Supporting Information), indicating enhanced dealumination in Na MX.<sup>[37]</sup> The survey spectra (Figure S2b of Supporting Information) show the presence of the Ti 3s signal in the Na MX sample, indicating a metallic state. The presence of free electrons also indicates enhanced conductivity, which will improve the electrochemical performance of the sample. The survey spectrum also indicates a reduction in the intensity of the F1s signal in the Na MX sample, which will also improve the redox activity of the sample.<sup>[38]</sup>

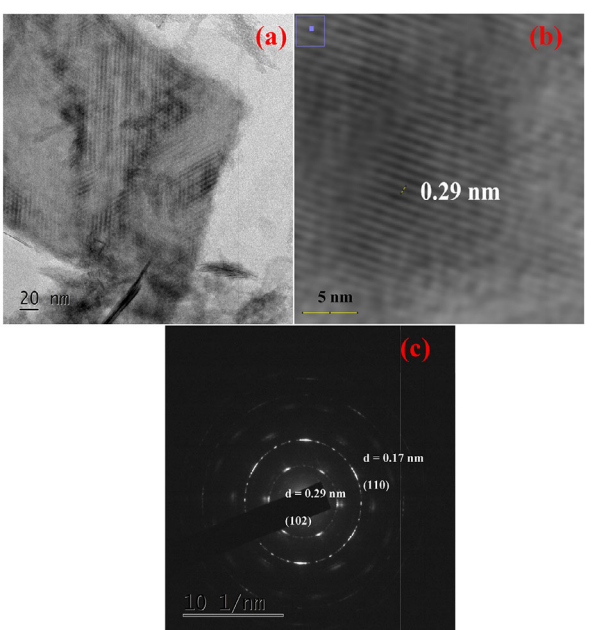


**Figure 6.** a) HR-TEM image of 0.04 Na MX, b) d spacing obtained from magnified HR-TEM image corresponding to the (102) plane, and c) SAED pattern confirming the (102) and (110) reflections.

HR-TEM studies (**Figure 6**) were carried out to analyze the crystallinity of the 0.04 Na MX sample. The HR-TEM reveals the layered morphology of the prepared sample. The selected area electron diffraction (SAED) confirms the polycrystalline

nature of the sample, consistent with the XRD results. The characteristic (110) and (102) planes were also identified from the SAED pattern.

A schematic illustration of the NaOH-assisted synthesis process and the removal of Al is shown in **Figure 7**.

The electrochemical properties of the optimized sample, 0.04 Na MX, were studied in a three-electrode setup. The cyclic voltammogram (CV) of multilayer MXene does not show redox peaks due to the close-packed layers and the inaccessibility of  $H^+$  ions to interact with Ti.<sup>[39]</sup> However, in delaminated MXene, the  $H^+$  ions can easily interact with Ti, resulting in the evolution of redox peaks.<sup>[37]</sup> A comparison of the CV of MX and 0.04 Na MX, given in the Supporting Information

(Figure S3), shows that the redox peak evolution is characteristic of NaOH-modified MXene, similar to delaminated MXene.<sup>[40]</sup> In multilayer MXene, the redox peak evolution cannot be obtained since the protons cannot intercalate into the multilayers.<sup>[36]</sup> The CV and galvanometric charge–discharge (GCD) of 0.04 Na MX, shown in **Figure 8**, exhibit the signature of redox reactions in the sample, similar to delaminated MXenes, even though additional steps for delamination have not been carried out in the present study.

This shows that additional delamination processes are not necessary when inherent delamination can be achieved by using cation-assisted synthesis of MXene. A specific capacitance of  $150\text{ F g}^{-1}$  was obtained for the 0.04 Na MX-coated carbon cloth

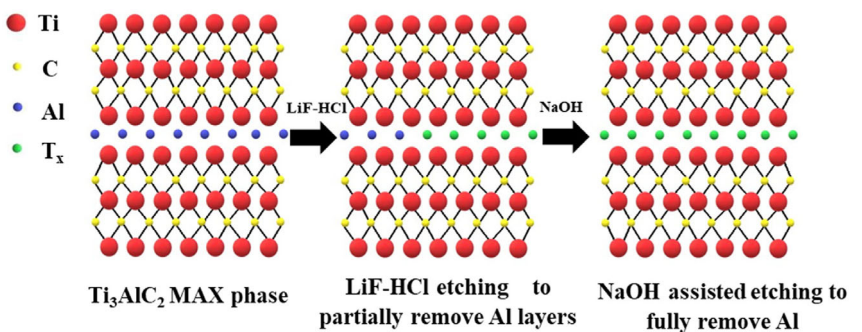


**Figure 7.** Schematic illustration of the NaOH-assisted dealumination in the sample.

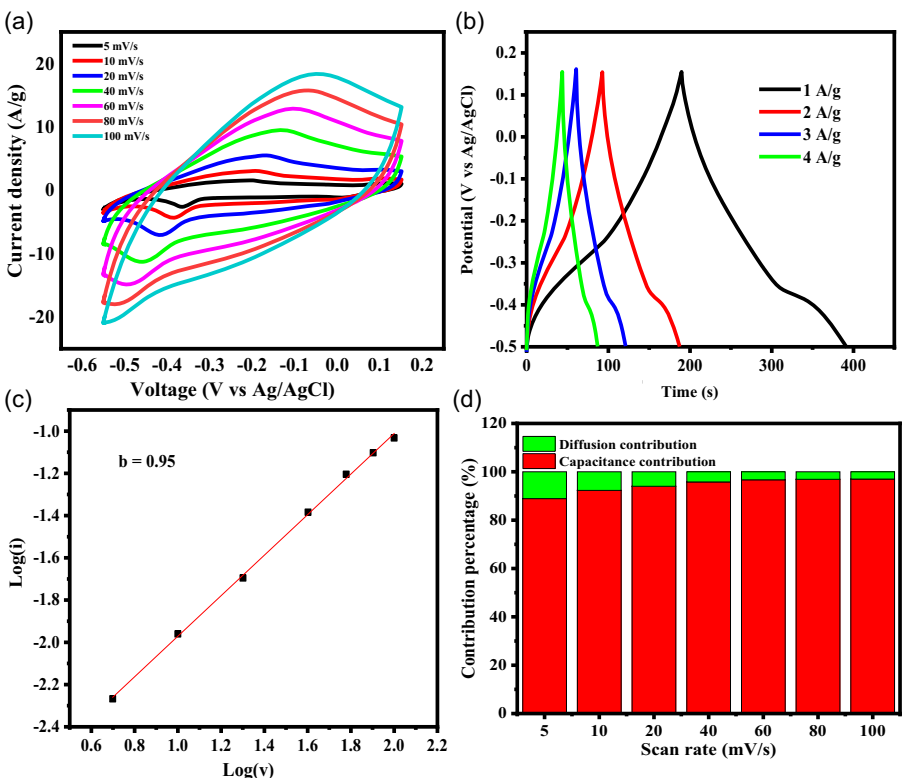


**Figure 8.** a) CV of 0.04 Na MX, b) GCD of 0.04 Na MX, c)  $\log(i)$  versus  $\log(v)$  graph to determine  $b$ , and d) fraction of contribution to the total charge stored from capacitive and diffusion processes.

electrode, with an active material weight of  $9 \text{ mg cm}^{-2}$ , using  $3 \text{ M H}_2\text{SO}_4$  as the electrolyte. The charge transport mechanism can be identified using the following equation

$$i = av^b \quad (5)$$

where  $v$  is the scan rate in  $\text{mV s}^{-1}$ ,  $i$  is the peak current in  $\text{mA g}^{-1}$  at various scan rates,  $a$  is a constant that takes into account the correct dimensionality of the equation, and the  $b$  value varies according to the contribution from different charge transfer mechanisms.  $b=1$  is indicative of the dominance of capacitive processes, and  $b=0.5$  is indicative of the dominance of diffusion-controlled processes; a  $b$  value between 0.5 and 1 indicates a combination of capacitive and diffusion-controlled processes. The  $b$  value is obtained as 0.95 for 0.04 Na MX from the slope of the  $\log(i)$  versus  $\log(v)$  graph, as shown in Figure 8c.

This suggests the dominance of capacitive processes over diffusion processes for charge transport. The exact contribution from capacitive and diffusion processes can be determined by employing the following equation<sup>[41]</sup>

$$i = k_1 v + k_2 v^{1/2} \quad (6)$$

The contribution fractions may be determined by calculating the value of  $k_1$  and  $k_2$  from the  $i/v^{1/2}$  versus  $v^{1/2}$  graph. The contribution fractions have been shown in Figure 8d. It may be observed that the obtained contribution from the capacitive process is greater than that of the diffusion contribution. The capacitance contribution increases from 88.9% at  $5 \text{ mV s}^{-1}$  to 97%

at  $100 \text{ mV s}^{-1}$ . Previous studies have shown that the redox properties associated with oxidation and reduction in cation intercalated MXene are not completely diffusion-controlled, and can be termed as a semi-diffusion-controlled process.<sup>[27]</sup> The present study confirms this fact, from the observed increase in capacitance contribution with the scan rate. According to the Grotthuss mechanism, confined water molecules between layers, forming structured water, can generate a rapid proton-transfer network.<sup>[42]</sup> The redox reactions mediated by confined water in the interlayers of MXene are fast-Faradaic reactions, unlike the diffusion processes in batteries. Hence, the capacitance contribution is more than the diffusion contribution. The inherent 2D layered nature and the enhanced interlayer spacing also provide easy access to the protons from the electrolyte to interact with the surface terminations.<sup>[43]</sup> Thus, the electrode exhibits surface-controlled kinetics, due to which the overall process can be termed as capacitive in nature.<sup>[39]</sup>

Symmetric supercapacitor devices using MXene alone in aqueous electrolytes pose limitations on the potential window of operation of the device, to 0.8 volts.<sup>[25]</sup> This necessitates the development of positive electrodes with compatible electrochemical properties to complement the performance of MXene in an asymmetric configuration.<sup>[44]</sup> RuO<sub>2</sub>, due to its inherent pseudocapacitive properties similar to MXene, was considered as the positive electrode. The XRD confirmed the formation of the rutile phase of RuO<sub>2</sub> (Figure S4a of Supporting Information), and the SEM image (Figure S4b of Supporting Information) confirmed a layered morphology, where spherical nanoparticles are

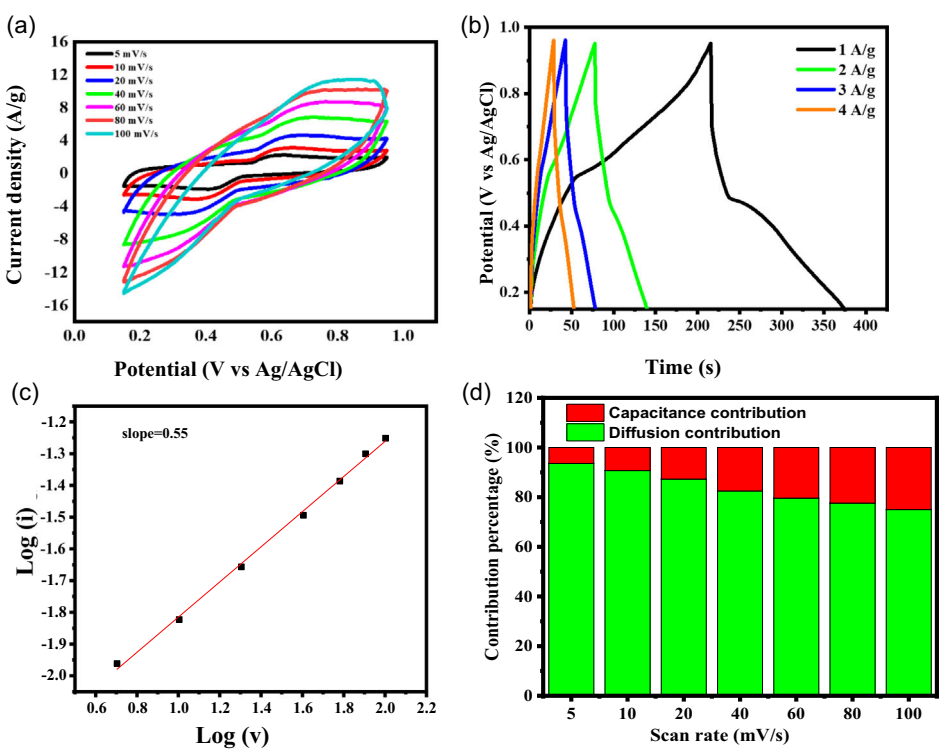
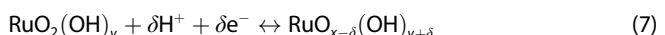


**Figure 9.** a) CV, b) GCD, c)  $\log(i)$  versus  $\log(v)$  graph to determine  $b$ , and d) fraction of contribution to the total charge stored from capacitive and diffusion processes of RuO<sub>2</sub>.

arranged to form layers. The pseudocapacitive nature of RuO<sub>2</sub> emerges from the interaction of Ru with the hydronium ions.<sup>[26]</sup> The electrochemical performance of RuO<sub>2</sub> was measured using a three-electrode configuration. The obtained CV and GCD are shown in Figures 9a,b, respectively. Similar to MXene, RuO<sub>2</sub> also exhibits pseudocapacitive behavior with the evolution of redox peaks.

The *b* value was obtained as 0.55, indicating a diffusion-dominant mechanism in RuO<sub>2</sub> (Figure 9c). The diffusion contribution is greater than the capacitive contribution as well (Figure 9d). The bulk Ru ions are also involved in the proton exchange, owing to which the diffusion contribution is high. The proton interaction of RuO<sub>2</sub> may be expressed by the following equation.



The specific capacitance of RuO<sub>2</sub> was 137.5 F g<sup>-1</sup> at 10 mV s<sup>-1</sup>. These specific capacitances and voltage windows of the materials were used in assembling an asymmetric supercapacitor, following mass-charge balancing.

$$m_+ C_+ V_+ = m_- C_- V_- \quad (8)$$

Asymmetric supercapacitors were assembled using RuO<sub>2</sub>, following the mass ratio obtained as per (Equation 8). The CV of the asymmetric supercapacitor using RuO<sub>2</sub> is shown in Figure 10a. The MXene/RuO<sub>2</sub> device had a specific capacitance of 73.3 F g<sup>-1</sup> at 5 mV s<sup>-1</sup>. It can be seen that, by virtue of two different electrode materials working in two different windows, an asymmetric device with the potential extendable to 1.5 volts, with a specific capacitance of 73.3 F g<sup>-1</sup>, energy density of 23 Wh kg<sup>-1</sup>, and power density of 796 W kg<sup>-1</sup> could be obtained. As ruthenium oxide is an expensive material, activated carbon was considered as a suitable alternative to pair with MXene. However, being an electric double-layer material, the performance of activated carbon was not comparable to that of MXene. The details of the study are given in the Supporting

Information, and Figure S5–S8 of the Supporting Information show the characterizations done using activated carbon.

The electrochemical characterization of MXene/RuO<sub>2</sub> asymmetric supercapacitor device is given in Figure 11. The CV and GCD of the device reflect the pseudocapacitive nature of MXene and RuO<sub>2</sub>. The Nyquist plot shows low charge transfer resistance for the device.<sup>[45]</sup> The equivalent series resistance is 1.6 ohms, and the charge transfer resistance is 1.8 ohms, obtained from the equivalent circuit fit shown in the inset of Figure 11c. The device had a cycling stability of 94.5% at the end of 2000 cycles at 500 mV s<sup>-1</sup>, which also indicates good rate capability of the device. The capacitance contribution and diffusion contributions were calculated using Dunn's equation, as shown in Figure 11e,f.<sup>[21]</sup> It can be seen that the device has a *b* value of 0.76, and the capacitive contribution increases gradually with scan rate. The capacitive contribution at 100 mV s<sup>-1</sup> is illustrated in Figure S9 of the Supporting Information, indicating dominance of capacitive behavior at high scan rates. The device exhibits a combination of the behaviors exhibited by individual electrodes, 0.04 Na MX and RuO<sub>2</sub>, with the *b* value lying between 0.55, obtained for the RuO<sub>2</sub> electrode, and 0.95, obtained for the 0.04 Na MX electrode.

The electrodes prepared using 0.04 Na MX and RuO<sub>2</sub> were used in the fabrication of an all-solid-state asymmetric supercapacitor (ASAS) device using PVA/H<sub>2</sub>SO<sub>4</sub> gel polymer electrolyte. The use of the gel polymer electrolyte enabled a further extension of the voltage window up to 2 V.

Figure 12 shows the CV and GCD of the prepared all-solid-state device. The device could be used to power an LED up to 2 volts. The lighting of the red LED using the assembled device in straight and bent architectures is given in the Supporting Videos 1 and 2, respectively, and photographs of the same are shown in Figure S10 of the Supporting Information, establishing the flexible nature of the prepared device. The CV of the ASAS remains intact at different scan rates from 5 to 500 mV s<sup>-1</sup>, indicating its high rate capability. The GCD of the device at 5 mA g<sup>-1</sup> is shown in Figure 12b, and the inset of Figure 12b shows the

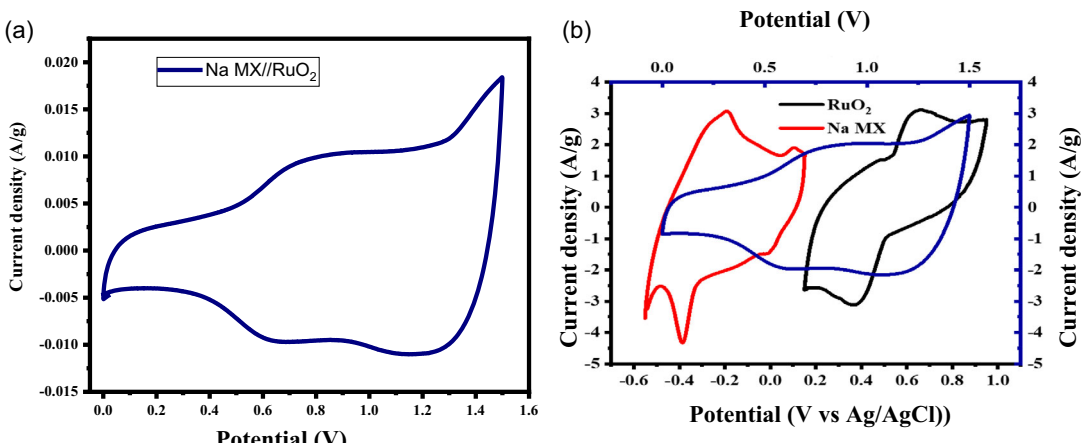


**Figure 10.** a) CV of the asymmetric device 0.04 Na MX//RuO<sub>2</sub> device. b) Comparison of the CV of the asymmetric device 0.04 Na MX//RuO<sub>2</sub> with that of 0.04 Na MX and RuO<sub>2</sub>.

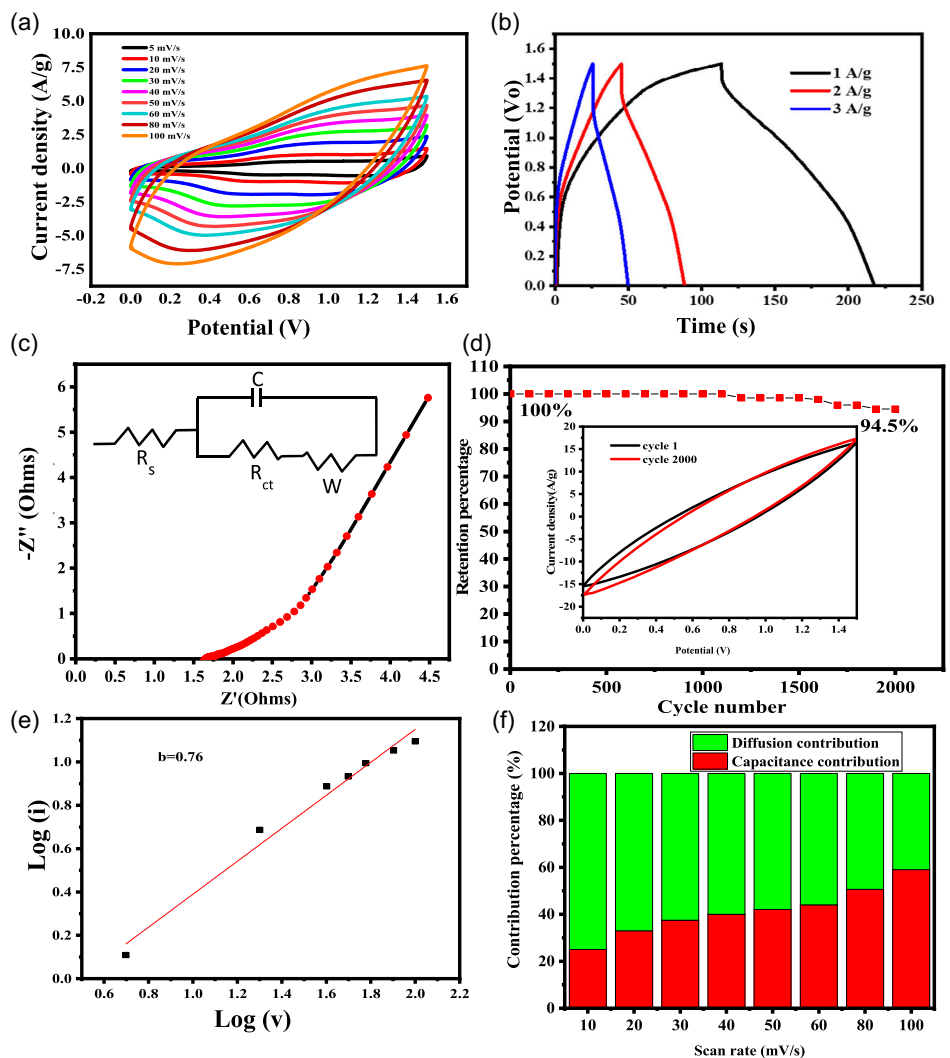


**Figure 11.** a) CV, b) GCD, c) Nyquist plot, d) cycling stability of asymmetric supercapacitor device, e)  $\log(i)$  versus  $\log(v)$  graph to determine value of  $b$ , and f) contribution fraction from capacitive and diffusion processes in charge storage.

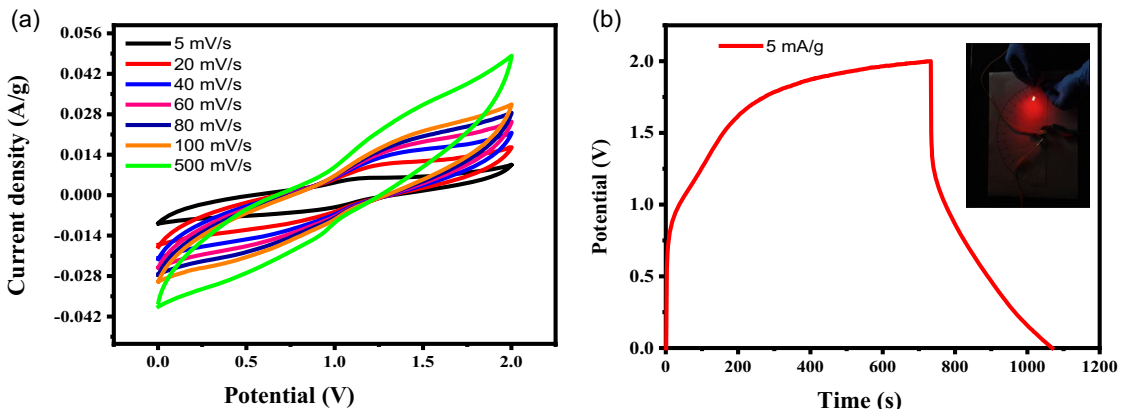


**Figure 12.** Electrochemical characterization of the all-solid-state asymmetric device. a) CV at various scan rates and b) GCD (inset shows the lighting of a single red LED with the all-solid-state asymmetric device).

capability of the device to power a red LED (included as Supporting Video), which shows the potential of the device in powering portable and flexible electronic devices. The device

exhibited appreciable specific capacitance of  $845 \text{ mF g}^{-1}$ , energy density of  $470 \text{ mWh kg}^{-1}$ , and power density of  $5000 \text{ mW kg}^{-1}$  at a current density of  $5 \text{ mA g}^{-1}$ .<sup>[42,43,46]</sup>

## 4. Conclusions

The study shows that the modification of the *in situ* HF forming technique using NaOH results in the formation of  $Ti_3C_2T_x$  MXene with enhanced removal of the Al from the MAX phase precursor  $Ti_3AlC_2$ . The enhanced structural properties of the synthesized material were confirmed using XRD, from the evolution of the intense (002) plane diffraction peak and the absence of the (104) plane diffraction peak. The morphology and functional analysis using SEM and Raman analyses were also consistent in confirming the enhancement in properties conferred by successful etching and inherent delamination processes. The inherent delamination was also reflected in the electrochemical characteristics of the material, with the evolution of redox peaks in the CV. The pseudocapacitive behavior could be brought out in the material without resorting to any additional delaminating steps, making the method simple and scalable. The produced MXene exhibits enhancement in characteristic properties, without compromising any of its inherent features. An asymmetric supercapacitor coupling MXene with  $RuO_2$  gave a specific capacitance of  $73.3\text{ F g}^{-1}$ , energy density of  $23\text{ Wh kg}^{-1}$ , and power density of  $796\text{ W kg}^{-1}$ . The fabricated ASAS device exhibited a specific capacitance of  $845\text{ mF g}^{-1}$ , energy density of  $470\text{ mWh kg}^{-1}$ , and power density of  $5000\text{ mW kg}^{-1}$  at a current density of  $5\text{ mA g}^{-1}$ . This shows the potential of the device in powering portable and flexible electronic devices.

## Acknowledgements

Author A.A. acknowledges RUSA for the RUSA SRF. The authors acknowledge RUSA 2.0 and UGC-DAE CSR for financial assistance, RUSA CUSATECH for the faculty exchange program, and Spanish Ministry of Science and Innovation/AEI under Project nos. PID2020-114796RB-(PROYECTO/AEI/10.13039/501100011033), MFA 2022/009 (SPINOD), and TED2021-132656B-C22, as well as to the Generalitat Valenciana (Conselleria d'Educació, Universitats i Ocupació) under Project nos. PROMETEU/2021/066 and PROMETEU/2021/082. The authors would also like to acknowledge access to the Servei Central de Suport a la Investigació Experimental (SCSIE) of the University of Valencia.

## Conflict of Interest

The authors declare no conflict of interest.

## Author Contributions

**Anamika Ashok:** data curation, methodology, investigation, writing—original draft preparation, writing—review and editing.  
**Varsha Vijayan:** data curation, methodology. **Shalu Mariam George:** data curation, methodology. **Aleena Tomy:** data curation, methodology. **Asha Arackal Sukumaran:** supervision, conceptualization, validation, methodology, writing—review and editing. **Oleksii Klymov:** resources (physical characterization—SEM, Raman).

**Vicente Muñoz-Sanjosé:** validation, writing—review and editing.  
**Mahesh Eledath Changarath and Juan F. Sánchez Royo:** resources (XPS measurements).

## Data Availability Statement

The data that support the findings of this study are available from the corresponding author upon reasonable request.

**Keywords:** asymmetric supercapacitor • etching • high mass loading • MXene • NaOH-modification

- [1] B. Anasori, Y. Gogotsi, *2D Metal Carbides and Nitrides (MXenes)*, Springer, Berlin 2019, <https://doi.org/10.1007/978-3-030-19026-2>.
- [2] M. Alhabeb, K. Maleski, B. Anasori, P. Lelyukh, L. Clark, S. Sin, Y. Gogotsi, *Chem. Mater.* **2017**, *29*, 7633.
- [3] Y. Li, H. Shao, Z. Lin, J. Lu, L. Liu, B. Dupoyer, P. O. Persson, P. Eklund, L. Hultman, M. Li, K. Chen, *Nat. Mater.* **2020**, *19*, 894.
- [4] P. Lian, Y. Dong, Z. S. Wu, S. Zheng, X. Wang, S. Wang, C. Sun, J. Qin, X. Shi, X. Bao, *Nano Energy* **2017**, *40*, 1.
- [5] D. Zhao, M. Clites, G. Ying, S. Kota, J. Wang, V. Natu, M. W. Barsoum, *Chem. Commun.* **2018**, *54*, 4533.
- [6] P. Zhang, K. Wang, H. Wang, D. Tan, C. Wang, X. Zhang, J. Zhu, *Electrochem. Commun.* **2023**, *157*, 107620.
- [7] T. Li, Y. Lulu, L. Qinglei, G. Jiajun, L. Ruichun, L. Jinghan, Y. Xudong, *Angew. Chem., Int. Ed.* **2018**, *57*, 6115.
- [8] X. Zang, J. Wang, Y. Qin, T. Wang, C. He, Q. Shao, H. Zhu, N. Cao, *Nano-Micro Lett.* **2020**, *12*, 77.
- [9] J. Pang, R. G. Mendes, A. Bachmatiuk, L. Zhao, H. Q. Ta, T. Gemming, H. Liu, Z. Liu, M. H. Rummeli, *Chem. Soc. Rev.* **2019**, *48*, 72.
- [10] A. S. Zeraati, S. A. Mirkhani, P. Sun, M. Naguib, P. V. Braun, U. Sundararaj, *Nanoscale* **2021**, *13*, 3572.
- [11] Z. S. Iro, C. Subramani, S. S. Dash, *Int. J. Electrochem. Sci.* **2016**, *11*, 10628.
- [12] M. E. Şahin, F. Blaabjerg, A. Sangwongwanich, *Energies* **2022**, *15*, 674.
- [13] K. S. Kumar, N. Choudhary, Y. Jung, J. Thomas, *ACS Energy Lett.* **2018**, *3*, 482.
- [14] J. Zhao, A. F. Burke, *Adv. Energy Mater.* **2021**, *11*, 1.
- [15] S.-W. Zhang, B.-S. Yin, X.-X. Liu, D.-M. Gu, H. Gong, Z.-B. Wang, *Nano Energy* **2019**, *59*, 41.
- [16] T.-B. Jiang, Z. Wen-Wen Zhang, W. Kai-Li Wu, W. Ming, W. Han-Min Wang, L. Wei, H. Qing-Xi, *Ind. Crops Prod.* **2022**, *187*, 115516.
- [17] P. J. Hall, E. J. Bain, *Energy Policy* **2008**, *36*, 4352.
- [18] T. Guo, D. Zhou, L. Pang, S. Sun, T. Zhou, J. Su, *Small* **2022**, *18*, 2106360.
- [19] X. Zang, C. Shen, M. Sanghadasa, L. Lin, *ChemElectroChem* **2019**, *6*, 976.
- [20] T. W. Lin, C. S. Dai, K. C. Hung, *Sci. Rep.* **2014**, *4*, 7274.
- [21] Y. Shao, M. F. El-Kady, J. Sun, Y. Li, Q. Zhang, M. Zhu, H. Wang, B. Dunn, R. B. Kaner, *Chem. Rev.* **2018**, *118*, 9233.
- [22] J. Huang, K. Yuan, Y. Chen, *Adv. Funct. Mater.* **2022**, *32*, 2108107.
- [23] M. Sajjad, M. I. Khan, F. Cheng, W. Lu, *J. Energy Storage* **2021**, *40*, 102729.
- [24] N. Jabeen, A. Hussain, Q. Xia, S. Sun, J. Zhu, H. Xia, *Adv. Mater.* **2017**, *29*, 1700804.
- [25] M. Rajkumar, C. T. Hsu, T. H. Wu, M. G. Chen, C. C. Hu, *Prog. Nat. Sci.: Mater. Int.* **2015**, *25*, 527.
- [26] J. P. Zheng, P. J. Cygan, T. R. Jow, *J. Electrochem. Soc.* **1995**, *142*, 2699.
- [27] A. Ashok, S. B. Saseendran, A. A. Sukumaran, *ACS Appl. Energy Mater.* **2024**, *7*, 5050.
- [28] A. Ashok, S. B. Saseendran, A. S. Asha, *Phys. Scr.* **2022**, *97*, 025807.
- [29] B. Anasori, M. R. Lukatskaya, Y. Gogotsi, *Nat. Rev. Mater.* **2017**, *2*, 16098.
- [30] Z. Li, L. Wang, D. Sun, Y. Zhang, B. Liu, Q. Hu, A. Zhou, *Mater. Sci. Eng., B* **2015**, *191*, 33.
- [31] O. Mashtalir, M. Naguib, B. Dyatkin, Y. Gogotsi, M. W. Barsoum, *Mater. Chem. Phys.* **2013**, *139*, 147.
- [32] A. Sarycheva, Y. Gogotsi, *Chem. Mater.* **2020**, *32*, 3480.

- [33] J. K. El-Demellawi, S. Lopatin, J. Yin, O. F. Mohammed, H. N. Alshareef, *ACS Nano* **2018**, *12*, 8485.
- [34] A. Zhou, Y. Liu, S. Li, X. Wang, G. Ying, Q. Xia, P. Zhang, *J. Adv. Ceram.* **2021**, *10*, 1194.
- [35] C. Shen, L. Wang, A. Zhou, B. Wang, X. Wang, W. Lian, Q. Hu, G. Qin, X. Liu, *Nanomaterials* **2018**, *8*, 80.
- [36] J. Chen, M. Chen, W. Zhou, X. Xu, B. Liu, W. Zhang, C. Wong, *ACS Nano* **2022**, *16*, 2461.
- [37] M. Ghidiu, M. R. Lukatskaya, M. Q. Zhao, Y. Gogotsi, M. W. Barsoum, *Nature* **2014**, *516*, 78.
- [38] A. G. Juandito, D. S. Khaerudini, S. Priyono, G. T. M. Kadja, D. Djuhana, M. Khalil, *J. Nanopart. Res.* **2024**, *26*, 110.
- [39] H. Shao, K. Xu, Y. C. Wu, A. Iadecola, L. Liu, H. Ma, L. Qu, E. Raymundo-Piñero, J. Zhu, Z. Lin, P. L. Taberna, P. Simon, *ACS Energy Lett.* **2020**, *5*, 2873.
- [40] C. Zhan, M. Naguib, M. Lukatskaya, P. R. C. Kent, Y. Gogotsi, D. E. Jiang, *J. Phys. Chem. Lett.* **2018**, *9*, 1223.
- [41] M. Karmakar, M. Swain, S. Punyasloka, B. Mondal, M. Noriyoshi, C. Ghoroi, *Mater. Chem. Phys.* **2025**, *331*, 130187.
- [42] D. Gandla, F. Zhang, D. Q. Tan, *ACS Omega* **2022**, *7*, 7190.
- [43] L. Li, N. Zhang, M. Zhang, L. Wu, X. Zhang, Z. Zhang, *ACS Sustainable Chem. Eng.* **2018**, *6*, 7442.
- [44] J. S. Ko, C. H. Lai, J. W. Long, D. R. Rolison, B. Dunn, J. N. Weker, *ACS Appl. Mater. Interfaces* **2020**, *12*, 14071.
- [45] R. Akhter, S. S. Makedar, *J. Materiomics* **2023**, *9*, 1196.
- [46] M. Cai, X. Wei, H. Huang, F. Yuan, C. Li, S. Xu, X. Liang, W. Zhou, J. Guo, *Chem. Eng. J.* **2023**, *458*, 141338.

---

Manuscript received: May 21, 2025

Revised manuscript received: August 27, 2025

Version of record online:

---